Science and Technology Facilities Council

Technical Report
STFC-TR-2026-006

SCARF Annual Report 2022–2023

P Pavelin, D Ross (editors)

February 2026

Enquiries concerning this report should be addressed to:

RAL Library
STFC Rutherford Appleton Laboratory
Harwell Oxford
Didcot
OX11 0QX

Tel: +44(0)1235 445577
email: library@stfc.ac.uk

Science and Technology Facilities Council reports are available online at:
https://epubs.stfc.ac.uk

Accessibility: a Microsoft Word version of this document (for use with assistive technology) may be available on request.

DOI: 10.5286/stfctr.2026006

ISSN 2753-5797

Science and Technology Facilities Council

SCARF Annual Report 2022-2023

Version: 1.0

Date: 19/02/2026

Editors:

Phil Pavelin (philip.pavelin@stfc.ac.uk) 01235 445141

Derek Ross (derek.ross@stfc.ac.uk) 01235 445651

Content written by the respective authors

Date	Revision	Changes
18/03/25	0.2	Tidied up for handover
19/03/26	0.9	Draft for approval complete
19/03/26	1.0	Final version

Abstract

Annual Report on the Usage and Scientific Impact of the SCARF Service

Dissemination

This is a public document

1. SCARF SERVICE

SCARF is a High-Performance Cluster for STFC staff, Facilities (ISIS, DIAMOND, CLF) and their users and collaborators. The SCARF Service was started in 2004 and has been upgraded year-on-year and now represents a significant capital investment in High Performance Computing. Overall SCARF now has approximately 699 nodes providing 16156 CPU cores and 113TB memory, underpinned by 5.5PB of disk space (Details in Appendix A1 and A2).

This report covers the period from 1 January 2022 to 31 December 2023 (henceforth referred to as 2022-2023) and outlines the research that SCARF has enabled.

SCARF Usage by Department

Each time a researcher uses the SCARF service the CPU time used is recorded. Jobs submitted to SCARF used 200 million CPU Hours during 2022-23.

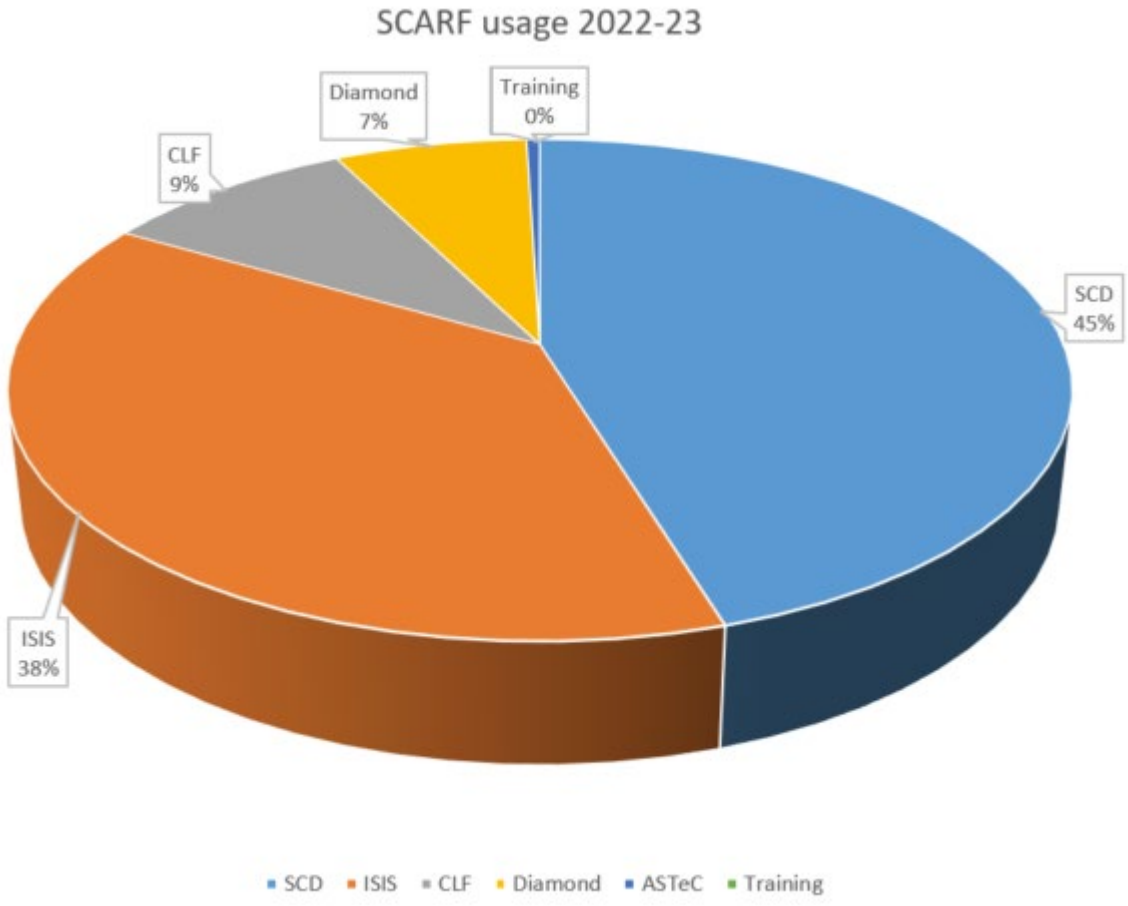

Fig. 1: Pie chart showing percentage usage of SCARF, by department

It is clear from the usage chart that ISIS and Scientific Computing are by far the heaviest users of SCARF with CLF, still a significant consumer of resources, next. Diamond, whilst still a relatively small user of SCARF, has maintained a steady level of usage.

A significant amount of computational resource has been utilised on SCARF and Section 3 highlights some of the scientific achievements that have been made possible with it.

SCARF Availability

We aim to keep SCARF available to users as much as possible.

SCARF provided good availability throughout this period. From time to time, there were scheduled maintenance periods, but these were advertised well in advance and kept to a minimum. A significant impact on SCARF's availability was reoccurring issues with the Panasas/Vdura storage system, components of the system were being ejected, causing the system to initiate a rebuild onto a spare component, slowing the performance. This was eventually mitigated by applying a fix from the vendor to reduce the frequency of the ejections.

Scheduled maintenance periods were advertised as far in advance as practicable and kept to a minimum.

Planned interventions in 2022

- Feb 10th - Rolling reboots of login nodes to apply security patches
- May 16th - Critical security update for Slurm
- June 18th - 19th - Planned network outage at RAL site
- July 14th - Rolling reboots of login nodes to apply security patches
- August 1st to 2nd - Upgrades to network switches and storage systems (Extended to August 5th due to issues with the storage system upgrade and further extended to August 8th due to power glitches affecting the RAL site)

Unplanned outages in 2022

- September 28th - Issue with GPFS storage system
- Oct 3rd to 5th - Continuing issue with GPFS storage system and issue with Panasas/Vdura storage system
- Oct 10th - Reoccurrence of Panasas/Vdura storage issue
- Oct 13th to 14th - Reoccurrence of Panasas/Vdura storage issue

Planned interventions in 2023

- January 9th -13th - Planned intervention to address issues with the Panasas/Vdura storage system
- April 25th - Rolling reboots of login nodes to apply security patches
- June 28th to 29th - Planned intervention to address issues with the Panasas/Vdura storage system (overlapped with occurrence of storage system issues)
- Oct 19th to 20th - R89 machine room five-yearly power testing phase 1 (no disruption to SCARF)
- Oct 28th to 29th - R89 machine room five-yearly power testing phase 2 (cluster was drained from 25th October and returned to service 1st November)

Unplanned outages in 2023

- April 24th to 25th - Reoccurrence of Panasas/Vdura storage issue
- December 18 to 19th - Reoccurrence of Panasas/Vdura storage issue

SCARF Developments

Major SCARF Developments are listed below:

- Introduction of the SCARF22 hardware, 32 nodes each with 32 physical cores provided by an AMD 7502p processor and 256G RAM, this is identical to SCARF21 and is available on the same HDR Infiniband fabric as SCARF21.
- Introduction of the SCARF23 hardware, this is 132 AMD 7502 32 core processor, and 4 GPU nodes with dual AMD 7302p 16 core processors and 4 NVIDIA A100 GPUs, this is identical to the SCARF21 and SCARF22 hardware and is also available on same the HDR IB fabric.
- Commencement of the migration from CentOS7 to Rocky9 Linux.

Application Highlights

SCARF maintains a large suite of applications for use by its users; a selection of significant application and versions added to the cluster over the period is documented in the table below

Application	Details
EPOCH v4.17	EPOCH is a plasma physics simulation code which uses the Particle in Cell (PIC) method.
FLUKA v2021.2	FLUKA is a fully integrated particle physics MonteCarlo simulation package.
RMCProfile v6.7.7	Reverse Monte Carlo for crystalline and disordered materials
GROMACS v2021.3	GROMACS is a molecular dynamics package mainly designed for simulations of proteins, lipids, and nucleic acids.
NWChem v7.0.2	NWChem is an ab initio computational chemistry software package which includes quantum chemical and molecular dynamics functionality.
QuantumESPRESSO v6.7	Quantum ESPRESSO is a suite for first-principles electronic-structure calculations and materials modelling.
Selected toolchains	• FOSS (GCC, OpenMPI, OpenBLAS, ScaLAPACK, FFTW) 2021a • OPMPI (Intel compilers, OpenMPI) 2021a • IOMKL (Intel compilers, OpenMPI, MKL) 2021a

Future Developments

- We plan to complete the migrate SCARF to Rocky Linux 9 during 2024.
- We are investigating the feasibility of allowing job submission to the SCD Cloud.

Help and Support

For any queries concerning the SCARF service, please email the SCARF Helpdesk

scarf@hpc-support.rl.ac.uk

PUBLICATIONS AND PRESENTATIONS

The publications and presentations for research that made use of SCARF are a way of measuring the impact that SCARF itself has.

Publications

A list of publications is given in Section 6.

Presentations

Scientists have presented their work at a wide range of international conferences (See Section 6). This helps to demonstrate that the science enabled by SCARF is world class.

SCIENCE HIGHLIGHTS

Impact of gas species on properties of self-injected electrons in a laser wakefield accelerator

L. R. Reid[1,2]

1. Accelerator Science and Technology Centre (ASTeC), UKRI STFC
2. Cockcroft Institute

The FEBE beam line will be dedicated to user applications of the CLARA accelerator at Daresbury laboratory. Some of these experiments may result in ionising radiation being created in addition to the electron beam from the accelerator itself. Understanding the possibilities is a critical aspect of the hazard analysis of the facility.

The addition of a 100 TW laser system which can be brought into the experimental area expands the range of experiments which can be conducted, including the development of plasma-based acceleration techniques where self-injection of an electron beam into a plasma wave can occur if the plasma density is high.

Particle-in-cell simulations with the code fbpic were run using the SCARF cluster with the expected parameters of the 100 TW laser which can be focused on a co-linear geometry with the CLARA electron beam. The initially neutral gas of the target was ionised by the laser using the ADK model. The density for each species was scaled to give a plasma density of 2×10^{18} cm^{-3}, close to threshold for injection with our laser parameters.

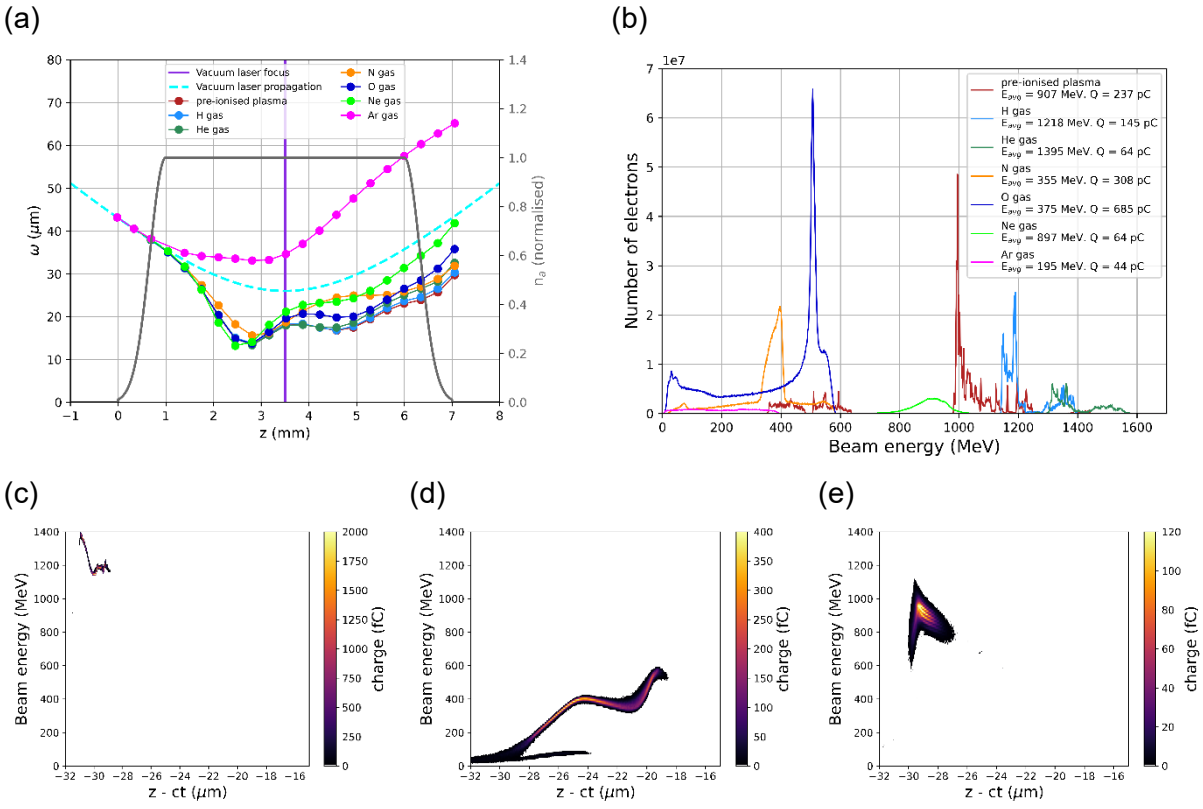

Fig. 2: (a) propagation of laser through gas for each species. (b) Energy spectrum of self-injected electron beam for each species. Corresponding phase space plots for (c) Hydrogen, (d) Nitrogen and (e) Neon.

The transverse intensity envelope of the laser can imprint itself on the level to which the atoms of a given gas are ionised, especially in the case of larger, more complex atoms. The plasma refractive index is a function of its electron number density which can result in it acting as a lens to the laser pulse propagating through it. This in turn affects the laser intensity and thus the strength of the accelerating field of the plasma wave in the wake of the laser. These variations in the levels of ionisation as well as the atomic structure also impact the amount of charge trapped inside the plasma wave and the mechanism by which it is trapped.

The propagation of the laser through the target for each gas species tested is shown in figure 2(a) where the laser spot size is compared to vacuum propagation. For most gasses, the laser spot falls smaller than vacuum propagation due to relativistic self-focusing but the radial plasma profile in the case of Argon (magenta) causes ionisation induced laser de-focusing.

Figure 2(b) shows the corresponding electron energy spectra of the injected beam at the exit of the plasma for each species. The differences in the propagation of the laser through the plasma and amount of trapped charge results in vastly different electron beams being observed. This is further illustrated in Fig. 2(c – e) which shows the longitudinal phase space of the injected electrons beams in the case of Hydrogen, Nitrogen and Neon.

For purposes of radiation hazard analysis, it is not appropriate to make decisions based on a single choice of gas species. The full range of options must be investigated to find the boundaries of beam energy, charge, divergence and spatial distribution.

Image segmentation when deep learning fails due to the lack of large training datasets: case study in computed tomography

Franck P. Vidal[1,2], Iwan Mitchell[2], Jean Michel Létang[3], Joël Lachambre[4], and Jean-Yves Buffière[4]

1. Scientific Computing, UKRI STFC
2. School of Computer Science & Engineering, Bangor University
3. Univ. Lyon, INSA-Lyon, Université Claude Bernard Lyon 1, UJM-Saint Étienne, CNRS, Inserm, CREATIS UMR 5220, U1294, F-69373 Lyon, France
4. INSA Lyon, CNRS, MATEIS UMR5510, France

Modern machine learning (ML) approaches often make use of deep learning (DL). It can be used in image segmentation, the process of assigning a label to each pixel of an image. A unique “label” is assigned to each segmented object. After segmentation, all the pixels belonging to the same object are grouped together, i.e. all the pixels of that object have the same value (the label).

The state-of-the-art DL techniques in image segmentation often rely on convolutional neural networks (CNNs). To avoid overfitting of the CNN models, large training datasets made of millions of segmented images are required. In many scientific applications there is no publicly available datasets: scientists must create their own training data. In image segmentation, images in the training dataset are manually labelled by domain experts, which is time consuming. This is not practical as the time available to label data is often limited. It is therefore not unusual that the size of the training dataset is too limited for DL approaches.

We propose to segment a CT scan of a section of electric cable. It was acquired with a laboratory CT device, the dual tube high energy (DTHE) scanner, at INSA-Lyon (France). The sample is made of two materials: copper and electric insulation (see Fig. 3). Beam hardening is visible where the copper wires are aligned in the original CT slice (see black pixels along this alignment in Fig. 4(a)). It makes it impossible to use typical image segmentation methods based on thresholding, region growing, watersheds, or traditional ML with image features. With such methods, copper was successfully segmented, but not other regions (see Fig. 4(b)). Tested CNNs were successful in segmenting the insulating material but failed to segment the copper wires (see Fig. 4(c)). We combine traditional supervised machine learning with deep learning to benefit from the advantages of both approaches whilst addressing their respective deficiencies (see Fig. 4(d)). The full imaging pipeline is as follows:

1. Take a computed tomography CT scan of a real object.
2. Reconstruct the CT volume.
3. Manually segment a few slices of the volume.
4. Extract image features for each pixel of the manually segmented slices.
5. Train a few traditional classifiers using the data from Step 4.
6. Select the “best classifier”.
7. Train a CNN on the manually segmented slices directly.
8. For each slice, for each pixel, apply the traditional classifier.
9. For each slice, for each pixel, apply the CNN classifier.
10. For each slice, for each pixel, combine the result of both classifiers.

Steps 5, 7, 8, 9 and 10 are time consuming and were performed using SCARF HPC facilities.

Fig. 3: Visualisation of the 3D model of the electric cable. Transparency is used to show the copper wires inside the insulating material.

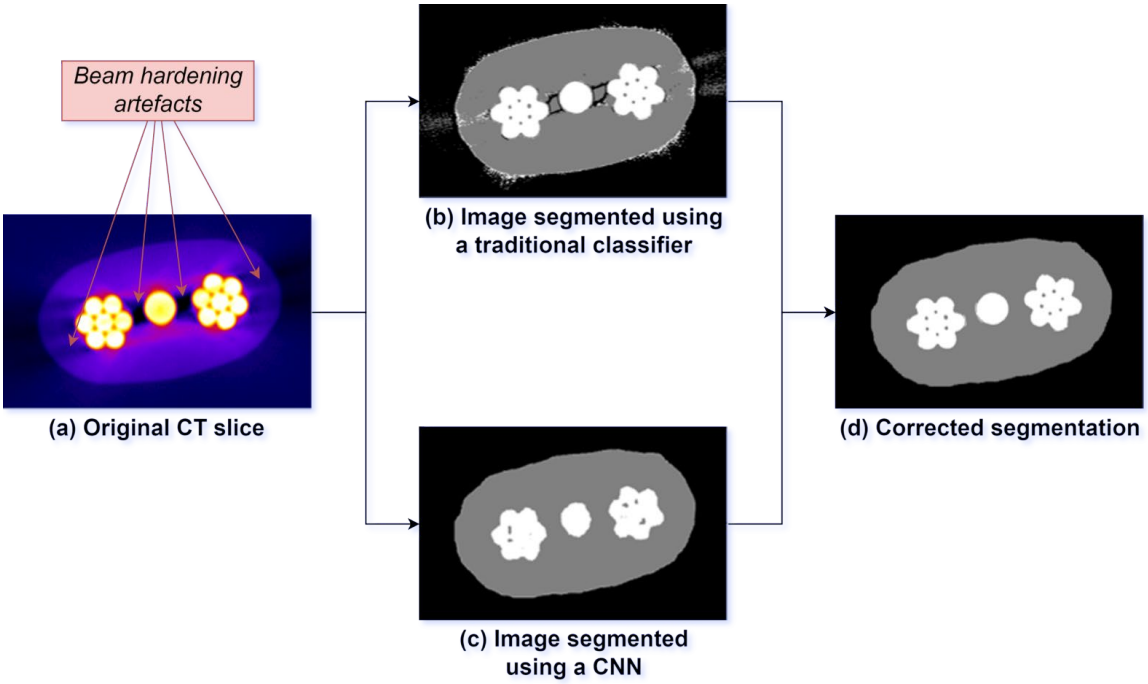

Fig. 4: Example of CT slice of a section of electric cable segmented using our method

Experimental and Modelling Studies of Local and Nanoscale para-Cresol Behaviour: A Comparison of Classical Force Fields

Katie Morton[1,2,3], Alin M. Elena[4], Alex O'Malley[1,3], Jeff Armstrong[2]

1. Institute for Sustainability, University of Bath
2. ISIS Pulsed Neutron and Muon Facility, UKRI STFC
3. UK Catalysis Hub
4. Scientific Computing, UKRI STFC

The dynamical behaviour of liquid p-cresol was studied using QENS combined with MD simulations to understand the behaviour of an important model component of biomass pyrolysis oil.

Two force field models, OPLS2005 and OPLS3, demonstrated accuracy in reproducing dynamical observables seen in the experiment. The QENS experiments observed jump diffusion and local isotropic rotational with activation energies of 22.7 $kJmol^{-1}$ and 10.1 $kJmol^{-1}$ respectively. MD simulations employing both OPLS2005 and OPLS3 models gave slower long-range diffusion rates than the experiment by factors of 2.0 and 3.8, respectively and slower rates of rotation were also observed by factors of 1.2 and 1.6 respectively.

We consider that the differences in rates are due to stronger intermolecular forces and higher system densities in the models, which are even more pronounced in the OPLS3 model with particularly strong "hydrogen bonding" observed.

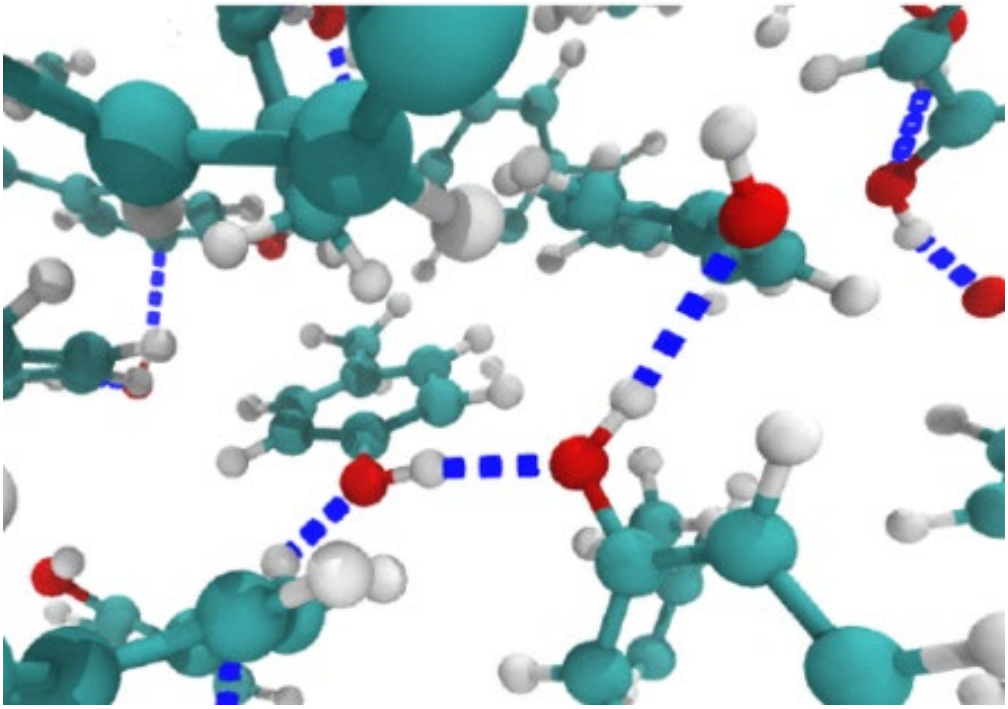

This work was published as *J. Phys. Chem. A*, 2023, **127**, 3305–3316.

The Effect of Molecular Shape and Pore Structure on Local and Nanoscale Cresol Behaviour in Commercial Zeolite Catalysts

Katie Morton[1,2,3], A. Porter[1], Jeff Armstrong[2] and Alex O'Malley[1,3]

1. Institute for Sustainability, University of Bath
2. ISIS Pulsed Neutron and Muon Facility, UKRI STFC
3. UK Catalysis Hub

The localised motions and longer range diffusivity of *m*- and *p*-cresol were studied in commercial zeolite catalysts H-Y and H-Beta using QENS experiments and classical MD simulations.

In the QENS experiments, observations were limited to isotropic rotation dynamics, rotating with frequencies from 3.3–5.6 × 10^{10} s^{-1} and with activation energies falling between 4.2–6.6 $kJmol^{-1}$ from 340–400 K. A higher proportion of molecules exhibited this motion within the larger-pore H-Y zeolite compared to H-Beta and with the more linear p-isomer compared to the m-isomer.

We conclude that cresol molecules rotate mainly within the larger channel intersections when residing in H-Beta. In general, as the proportion of mobile molecules increases from H-Beta to H-Y the average rate of rotation decreases, attributed to increased cresol-cresol interactions. The same motion was reproduced by classical MD simulations. Comparable proportions of mobile populations and rotational coefficients (5.7–8.5 ×10^{10} s^{-1}) were noted in each system showing the same trends and close to within error of the QENS measurements. Accessing higher energy transfer ranges inaccessible to the QENS instrument revealed a rapid rattling motion of cresols H-bonded to acid sites or partially trapped by the zeolite framework or adjacent cresol.

Due to the excellent level of agreement between the simulation and experiment, the capability of MD simulations to explore longer timescales allowed the observation of restricted cresol diffusion from 0.4–6.5 ×10^{-10} m^2s^{-1}, and higher activation energies from 20.1–31.6 $kJmol^{-1}$. p-cresol in H-Beta showed unexpectedly fast diffusion due to the inability of the longer molecules to form many hydrogen bonds with an optimal 180° bonding angle and diffusing parallel to the channel.

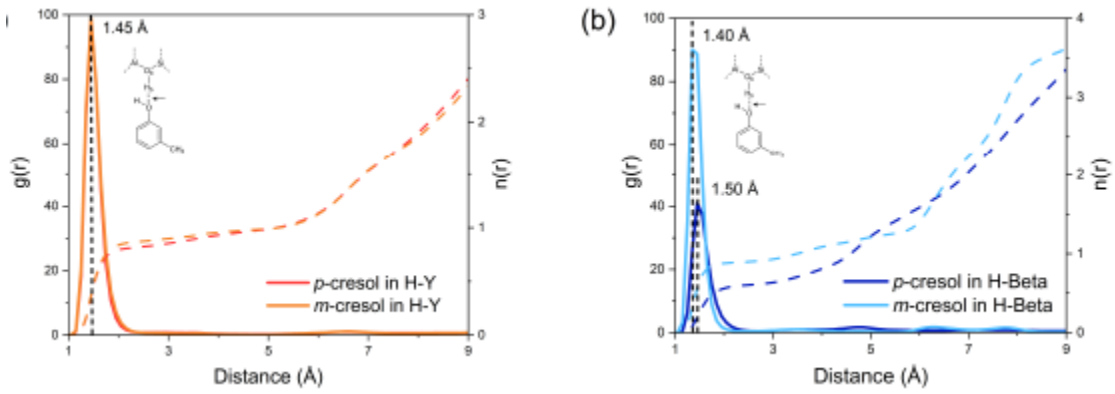

Fig. 5: The RDFs (g(r)) showing the bonding probability between cresol hydroxyl groups and the zeolite acid site show a significant decrease in the probability and length of bonding occurring for p-cresol in H-Beta.

Additional simulations operating at a catalytically relevant temperature (653 K) revealed faster diffusion and reduced adsorption to the BASs. Incorporating a smaller pore HZSM5 zeolite we observed diffusion that was slower by 1–2 orders of magnitude than that of the larger pore zeolites, attributed to confinement effects rather than acid site interactions. Consequently, to understand the internal diffusion rates of cresols throughout zeolite pores, the interplay between the molecule:zeolite pore diameter ratios and acid site strengths and densities must be considered.

Unravelling the Ordered Phase of the Quintessential Hybrid Perovskite MAPbI3 – Thermophysics to the Rescue

Pelayo Marin-Villa[1], Ana Arauzo[2], Kacper Druzbicki[1,3], and Felix Fernandez-Alonso[1,4,5]

1. Materials Physics Center, CSIC-UPV/EHU, Spain
2. Instituto de Nanociencia y Materiales de Aragón (INMA), CSIC-Universidad de Zaragoza, Spain
3. Centre of Molecular and Macromolecular Studies, Polish Academy of Sciences, Poland
4. Donostia International Physics Center (DIPC), Spain
5. IKERBASQUE – Basque Foundation for Science, Spain

In the light of the growing need for improved photovoltaic and optoelectronic materials, hybrid organic−inorganic perovskites (hereafter HOIPs) stand out as exceedingly promising candidates. They offer exceptional conversion efficiencies and coherent photocarrier transport typical of classic crystalline inorganic semiconductors [1,2], yet at the same time they also exhibit rather unusual nuclear dynamics reminiscent of that seen in liquids [3,4]. While understanding their atomic structure and dynamics is critical to both rationalize their exceptional photovoltaic performance and improve their environmental and operational stability [5], this task remains a formidable endeavour that has to date met with limited success.

Our work pioneers the use of specific heat data to scrutinize further the validity of two models of the cation-ordered phase of MAPbI3 (pseudo-orthorhombic *P1* and orthorhombic *Pnma*) described in our previous works [6,7]. Using these thermophysical data alongside phonon calculations obtained with plane-wave density functional theory (PWDFT), we introduce a joint experimental−computational protocol allowing for a quantitative validation of candidate structural models of HOIPs. Our calculated phonon band structures grant us with the opportunity to provide quantitative predictions for the temperature dependence of the heat capacity within the harmonic approximation (see Figure 6) and to compare these with the experimental data.

By focusing on how low energy modes primarily associated with the inorganic framework manifest themselves in the behaviour of the specific heat, it was possible to prove that the *P1* structure provides an improved description of the structure of the ordered phase of MAPbI3 at ambient pressure, relative to what has been inferred from crystallographic studies to date. We also anticipate that the realm of applicability of this technique could be further extended to the study of other more complex HOIPs and their mixtures.

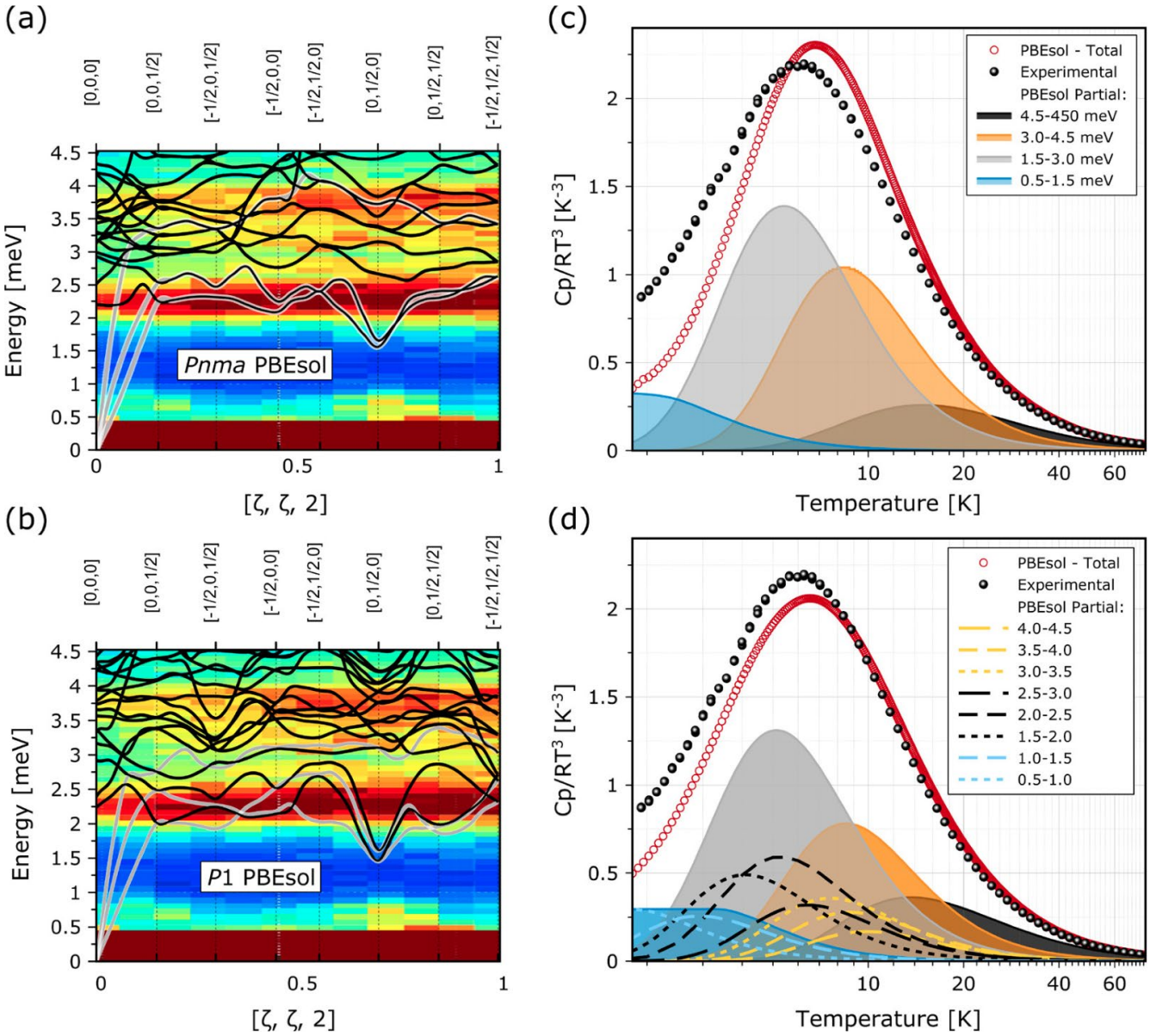

Fig. 6: (left panels) Calculated phonon dispersion relations for the Pnma (a) and P1 (b) models. The resulting phonon branches are presented in the range 0−4.5 meV and overlaid on the color maps corresponding to INS data from a hydrogenous single-crystal specimen.4 (right panels) Experimental (black dots) and theoretical (red dots) Cp(T)/T3. Partial contributions to this quantity from different phonon energy intervals are represented by the shaded curves, as defined in panel c. For the P1 model, these contributions are decomposed further by using 0.5 meV intervals, as shown by the broken lines in (d).

References

[1] Gonzalez-Pedro, V.; Juarez-Perez, E. J.; Arsyad, W.-S.; Barea, E. M.; Fabregat-Santiago, F.; Mora-Sero, I.; Bisquert, J. General Working Principles of CH3NH3PbX3 Perovskite Solar Cells. Nano Lett. 2014, 14, 888−893.

[2] Ferreira, A. C.; Létoublon, A.; Paofai, S.; Raymond, S.; Ecolivet, C.; Rufflé, B.; Cordier, S.; Katan, C.; Saidaminov, M. I.; Zhumekenov, A. A.; et al. Elastic Softness of Hybrid Lead Halide Perovskites. Phys. Rev. Lett. 2018, 121, 1−12.

[3] Miyata, K.; Atallah, T. L.; Zhu, X. Y. Lead Halide Perovskites: Crystal-liquid Duality, Phonon Glass Electron Crystals, and Large Polaron Formation. Sci. Adv. 2017, 3, 1−11.

[4] Ferreira, A. C.; Paofai, S.; Letoublon, A.; Ollivier, J.; Raymond, S.; Hehlen, B.; Ruffle, B.; Cordier, S.; Katan, C.; Even, J.; Bourges, P. Direct Evidence of Weakly Dispersed and Strongly Anharmonic Optical Phonons in Hybrid Perovskites. Commun. Phys. 2020, 3, 1−10.
[5] Mozur, E. M.; Neilson, J. R. Cation Dynamics in Hybrid Halide Perovskites. Annu. Rev. Mater. Sci. 2021, 51, 269−291.

The heating of hot electrons produced at sub-relativistic intensities.

R. A. B. Alraddadi[1], A. . L. Robinson[2], Raoul M. G. M Trines[2] and N. C. Woolsey[3].

1. Physics Department, Science Colleges, King Saud University, Riyadh, Saudi Arabia
2. Central Laser Facility, UKRI STFC
3. York Plasma Institute, Department of Physics, University of York, York

Understanding the physical mechanisms of laser-generated fast electron heating is crucial for different areas of high energy density physics. As MeV energetic electrons have their limitations in the term of plasma heating [1,2], we proposed alternative fast-electron-heating approach supported by analytic method [3]. Our approach uses lower energy 'hot' electrons in the range of 20 keV to 100 keV that can be produced at sub-relativistic intensities.

We use SCARF-derevolutionibus resources to run sets of two-dimensional PIC simulations, namely EPOCH code to estimate the required conditions for such heating. Hot electrons are generated via inducing Two-Plasmon Decay (TPD) instabilities [kruer2019physics]. Figure 7 shows the emerging of TPD instability where electron jets features with 45°. We found that 10% of the absorption fraction and 30 keV are enough to boost hot electron heating and longer density scale length is needed to increase absorption fraction.

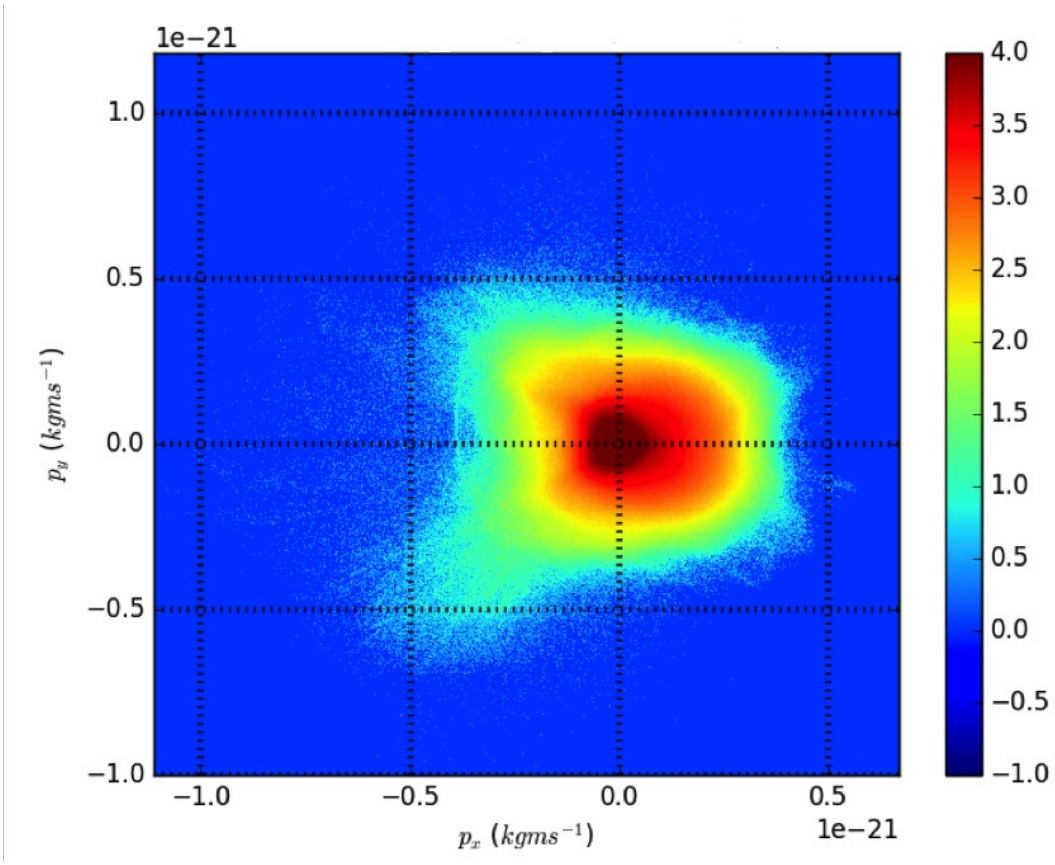

Fig. 7: The electron phase-space plot px-py.

References

[1] A. R. Bell et al, *Plasma Phys.Control. Fusion*, 39, 653 (1997).
[2] P. Patel et al, *Physical review letters*, 91, 125004 (2003).
[3] R. A. B. Alraddadi, A. P. L. Robinson, Raoul M. G. M Trines, and N. C. Woolsey, Phys. Plasmas, to be submitted (2024).
[4] W. Kruer, The physics of laser plasma interactions, (crc Press, 2019)

Investigating wetted foam capsules for inertial fusion energy

R W Paddock[1,2] et al

1. Department of Physics, Atomic and Laser Physics Sub-Department, Clarendon Laboratory, University of Oxford
2. Department of Engineering Science, University of Oxford

In inertial fusion, a capsule containing DT fuel is compressed to extreme densities and temperatures via irradiation by high power lasers. The DT ions can then undergo fusion, and if the densities/temperatures are sufficiently high, the energy produced by these fusion reactions can be greater than the energy used to drive the implosions. While significant progress has been made in this field in recent years, further improvements are required to improve the fusion performance to a level where it could be suitable for power generation.

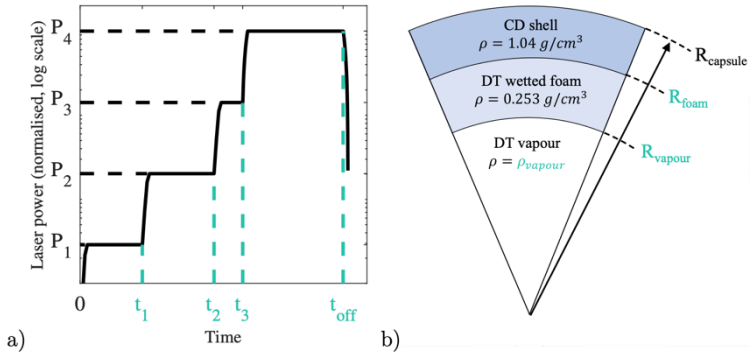

Fig. 8: a) The laser pulse profile and b) the capsule design for the wetted foam implosions simulated in the 2021 campaign. The variables shown in teal were optimised through the simulation campaign to maximise the fusion performance.

One such potential improvement is the use of wetted-foam capsules, where the DT fuel is a liquid that has saturated a low-density carbon foam structure. Along with potential performance benefits, such capsules could potentially be mass-manufactured at low cost – a necessity for a future fusion reactor.

SCARF has been used to run a series of simulation campaigns over the last few years to investigate the potential fusion performance of such capsules. A first campaign in 2021 optimised a series of different wetted-foam implosions, exploring the potential energy outputs that could be achieved using implosions of such capsules in a predicted low-instability regime. Further simulation campaigns have explored the effect of changing the frequency of the laser driver, and of applying the novel ‘auxiliary heating’ technique to such implosions. Here, a relativistic electron beam is used to heat the central ‘hotspot’ of the implosion, increasing the temperature just prior to the time of peak compression. These simulations have shown that this technique can substantially improve fusion performance and have been instrumental in developing a simple model to explain the increase in performance from this technique.

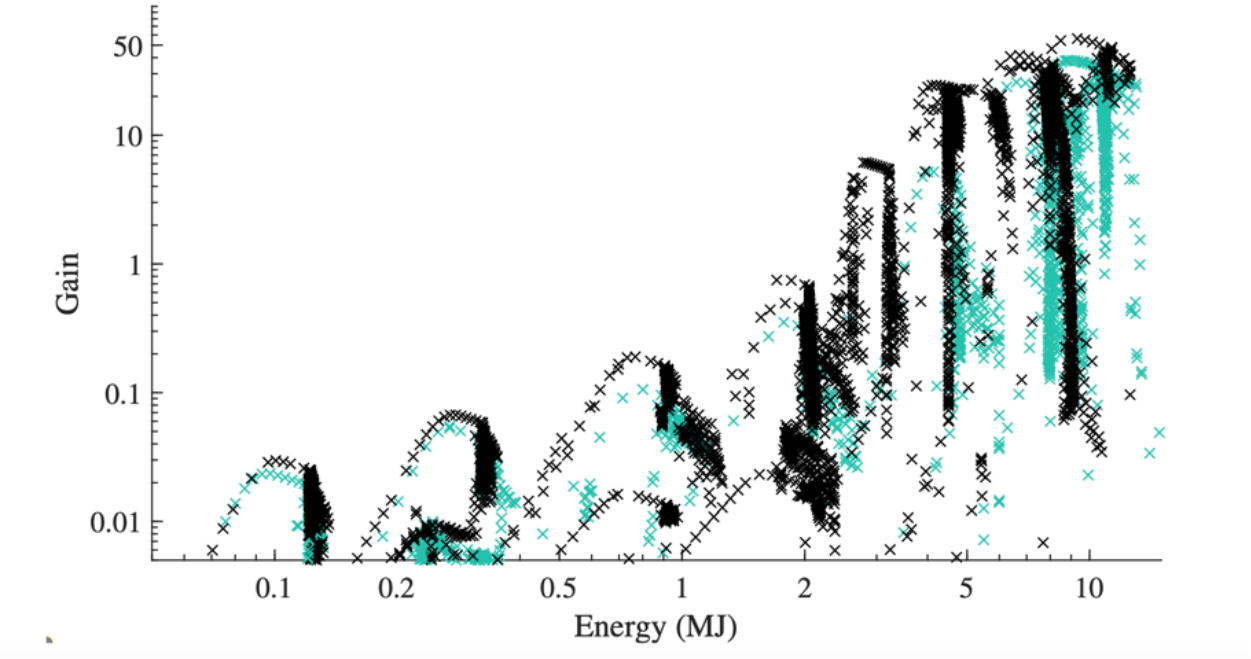

Fig. 9: Gain (output energy divided by input energy) vs laser energy for over 10,000 simulations of wetted foam implosions performed on SCARF.

Publications

- R. W. Paddock et al., "One-dimensional hydrodynamic simulations of low convergence ratio direct-drive inertial confinement fusion implosions", Philosophical Transactions of the Royal Society A: Mathematical, Physical and Engineering Sciences, **379**, 20200224 (2021).

- R. W. Paddock et al., "Pathways towards break even for low convergence ratio direct-drive inertial confinement fusion", Journal of Plasma Physics, **88**, 905880314 (2022).

- R. W. Paddock et al., “Energy gain of wetted-foam implosions with auxiliary heating for inertial fusion studies”, Plasma Phys. Control. Fusion, **66,** 025005 (2024).

Selected conferences

- R.W. Paddock – Direct Drive and Fast Ignition Workshop, 2022

- R.W. Paddock – American Physical Society Division of Plasma Physics 2021, 2023

Structural Dynamics of Chloromethanes through Computational Spectroscopy: Combining INS and DFT

Mariela M. Nolascoa[1], Mariana Coimbra de Almeida[1], Stewart F. Parker[3], Pedro D. Vaz,[2] and Paulo Ribeiro-Claroa[1]

1. CICECO – Aveiro Institute of Materials, Departament of Chemistry, University of Aveiro
2. Champalimaud Foundation, Champalimaud Centre for the Unknown, Lisboa, Portugal
3. ISIS Neutron & Muon Source, UKRI STFC

In this work[1], the structural dynamics of the chloromethanes CCl_4, $CHCl_3$ and CH_2Cl_2 was evaluated through a computational spectroscopy approach, by comparing experimental inelastic neutron scattering (INS) spectra with the corresponding simulated spectra obtained from periodic DFT calculations.

The overall excellent agreement between experimental and calculated spectra (Figure 10) allows a confident assignment of the vibrational features, including not only the molecular fundamental modes, but also lattice and combination modes. In particular, an impressive overtone sequence for $CHCl_3$ is fully described by the simulated INS spectrum. In the CCl4 spectrum, the splitting of the v3 mode at ca. 765-790 cm^{-1} is discussed on the basis of Fermi resonance vs. crystal splitting controversy. This work was presented at SiMol2023, Oxfordshire, UK.

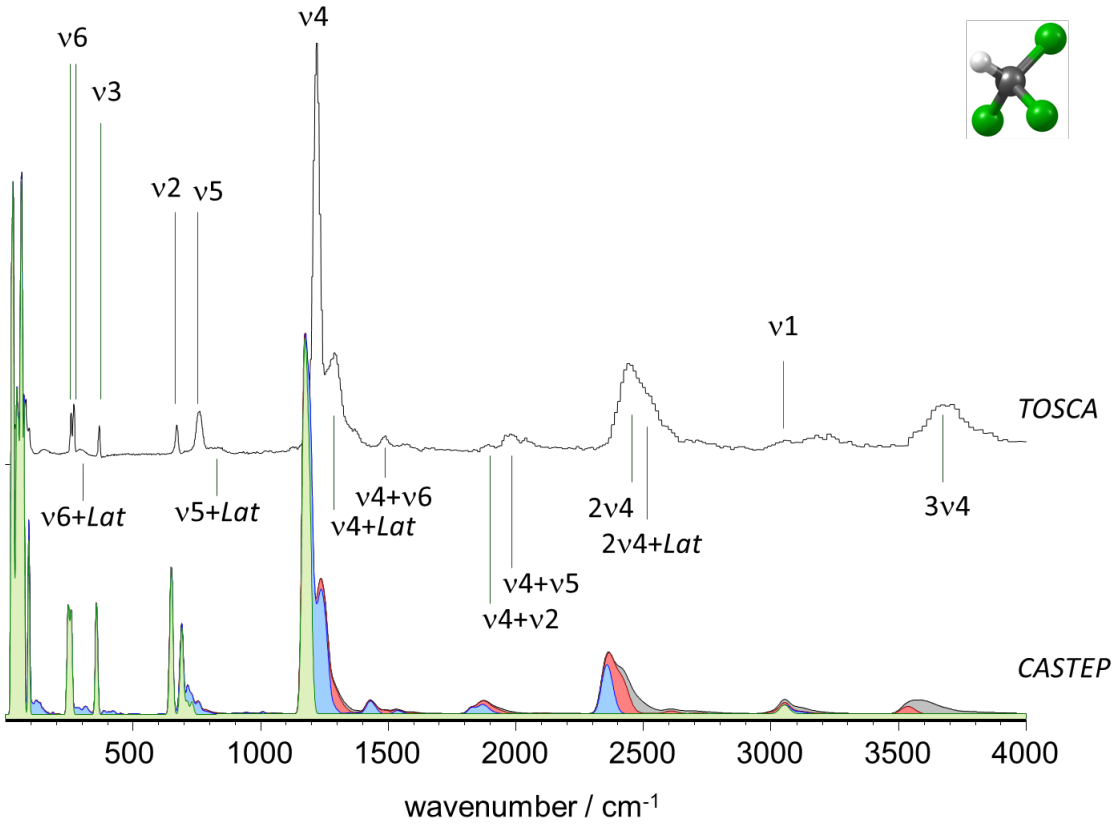

Fig. 10: The INS spectra of trichloromethane (chloroform) up to 4000 cm^{-1}: Experimental (top, TOSCA) and simulated from periodic calculations (bottom, CASTEP). Colours indicate the intensity contributions from fundamental modes (green), two-quanta events (blue), three-quanta events (red), and higher order quantum events (grey).

References

[1] Nolasco, M. M., Coimbra, M. M., Parker, S. F., Vaz, P. D. & Ribeiro-Claro, P. J. A. Structural Dynamics of Chloromethanes through Computational Spectroscopy: Combining INS and DFT. *MOLECULES* **27** (2022), 7661; DOI: 10.3390/molecules27217661.

Exploring asymmetry induced entropy in tetraalkylammonium–urea DES systems: what can be learned from inelastic neutron scattering?

Catarina F. Araujo[1], Paulo Ribeiro-Claro[1], Pedro D. Vaz[2], Svemir Rudic[3], Rafael A. F. Serrano[1], Liliana P. Silva[1], J. A. P. Coutinho[1] and Mariela M. Nolasco[1]

1. CICECO – Aveiro Institute of Materials, Department of Chemistry, University of Aveiro
2. Champalimaud Foundation, Champalimaud Centre for the Unknown, Lisboa, Portugal
3. ISIS Neutron & Muon Source, UKRI STFC

In this work[1], inelastic neutron scattering (INS) spectroscopy is used to investigate the impact of entropic factors on the behaviour of deep eutectic solvents (DES). Periodic density functional theory calculations (DFT) provide a reliable assignment of the vibrational modes of pure compounds. This assignment guides the analysis of INS spectra of binary mixtures – with particular attention to methyl torsional modes. Deviations from ideality in the mixtures of tetraalkylammonium salts with urea are readily determined through a simplified thermodynamic approach.

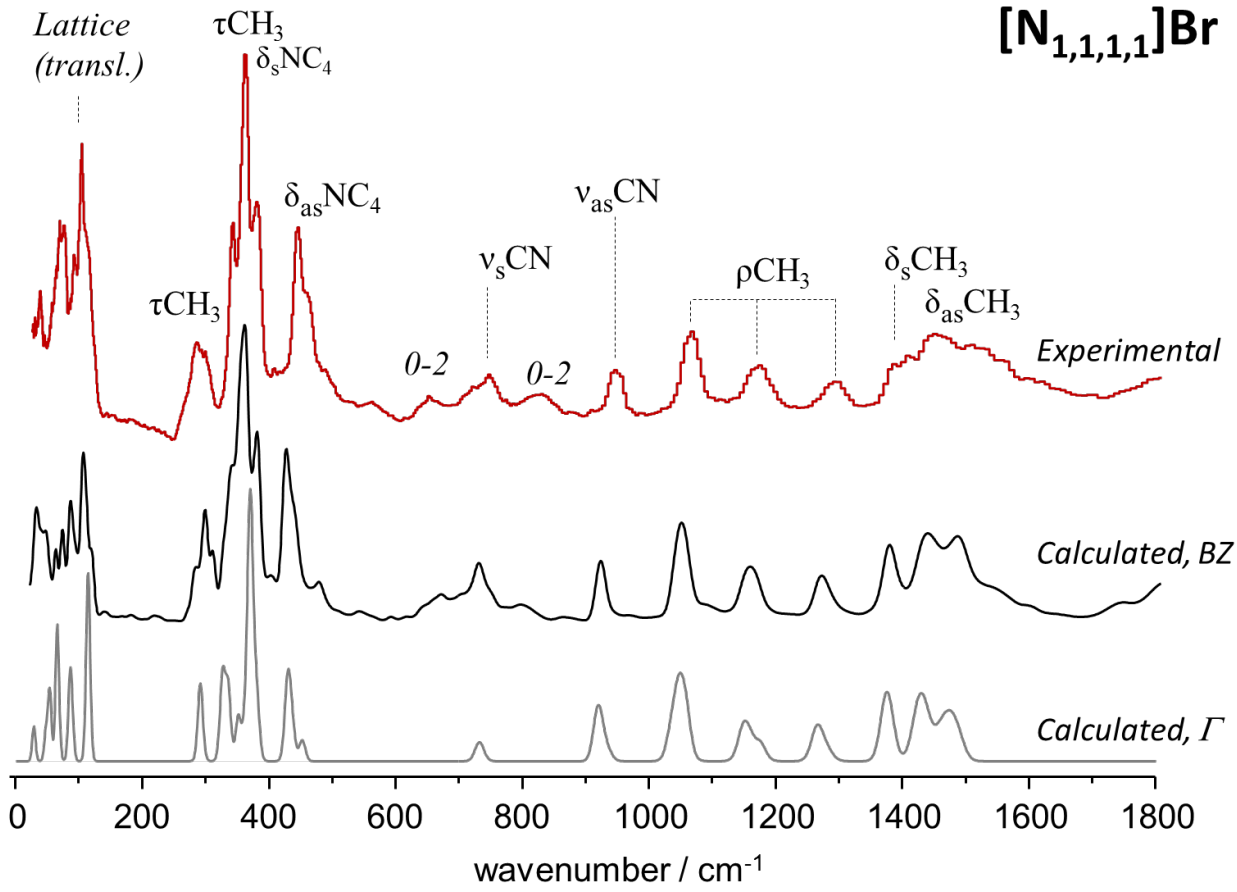

Fig. 11: Experimental (top line, red) and calculated (middle, bottom) spectra for tetramethyl-ammonium bromide, [$N_{1,1,1,1}$]Br. Bottom line shows the fundamental transitions at the Γ-point, while the middle line includes dispersion over the Brillouin zone. Experimental spectrum from TOSCA database

This study reports and discusses the relationship between the cation's asymmetry, the INS spectra of the eutectic mixture and its deviation from ideality. Contrary to the majority of systems studied so far, the deep eutectic system comprised of [$N_{2,2,2,1}$]Cl and urea appears to owe its deviation from ideality to entropic rather than enthalpic factors. In this way, it can be concluded that INS spectroscopy discloses the asymmetry induced entropy factors in

tetraalkylammonium:urea mixtures and emerges as a useful tool in the study of entropy as a driver of deep eutectic formation. This work was presented at SiMol2023, Oxfordshire, UK.

References

[1] Nolasco, M. M. *et al.* Exploring asymmetry-induced entropy in deep eutectic solvents. *STFC ISIS Neutron Muon Source* (2018). DOI:10.5286/ISIS.E.RB1810054

Shedding Light on Cuprorivaite, the Egyptian Blue Pigment: Joining Neutrons and Photons for a Computational Spectroscopy Study

M. M. Coimbra[1], I. Martins[1], S.M. Bruno[1], P. D. Vaz[2], P. Ribeiro-Claro[1], S. Rudić[3], and M. M. Nolascoa[1]

1. CICECO – Aveiro Institute of Materials, Department of Chemistry, University of Aveiro
2. Champalimaud Foundation, Champalimaud Centre for the Unknown, Lisboa, Portugal
3. ISIS Neutron & Muon Source, UKRI STFC

The unique properties of Egyptian blue, a cuprorivaite pigment, were herein studied[1] through a holistic computational and experimental approach. A reliable model of the crystal of cuprorivaite was obtained through periodic-DFT calculations (performed using SCARF computational facilities with the CASTEP code), allowing for the elucidation of its lattice dynamics, including assessment of structural, electronic and vibrational properties.

From this model, a sound assignment of the inelastic neutron scattering spectrum was obtained (Figure 12 below), along with estimated values of heat capacity and Debye temperature, band-gap values and magnetic properties of the crystal. Inelastic neutron scattering and diffuse reflectance infrared Fourier transform spectroscopies provided enlightenment on the chemical surfaces of the pigment Egyptian blue – which was missing hitherto and is critical for potential applications of the pigment, such as those involving host-matrix interactions or requiring surface derivatization, – while confirming the simulation results. On that account, it was found that the intensity of the dangling νSiO_d mode is ca. 8%-13% of total νSiO modes. Moreover, and regarding the electronic properties, the band structure confirmed that $CaCuSi_4O_{10}$ is a direct band gap semiconductor, with the Valence Band Maximum (VBM) and the Conduction Band Minimum (CBM) located at the Γ-point, in both the alpha (spin-up) and beta (spin-down) density bands. This work was presented at SiMol2023, Oxfordshire, UK.

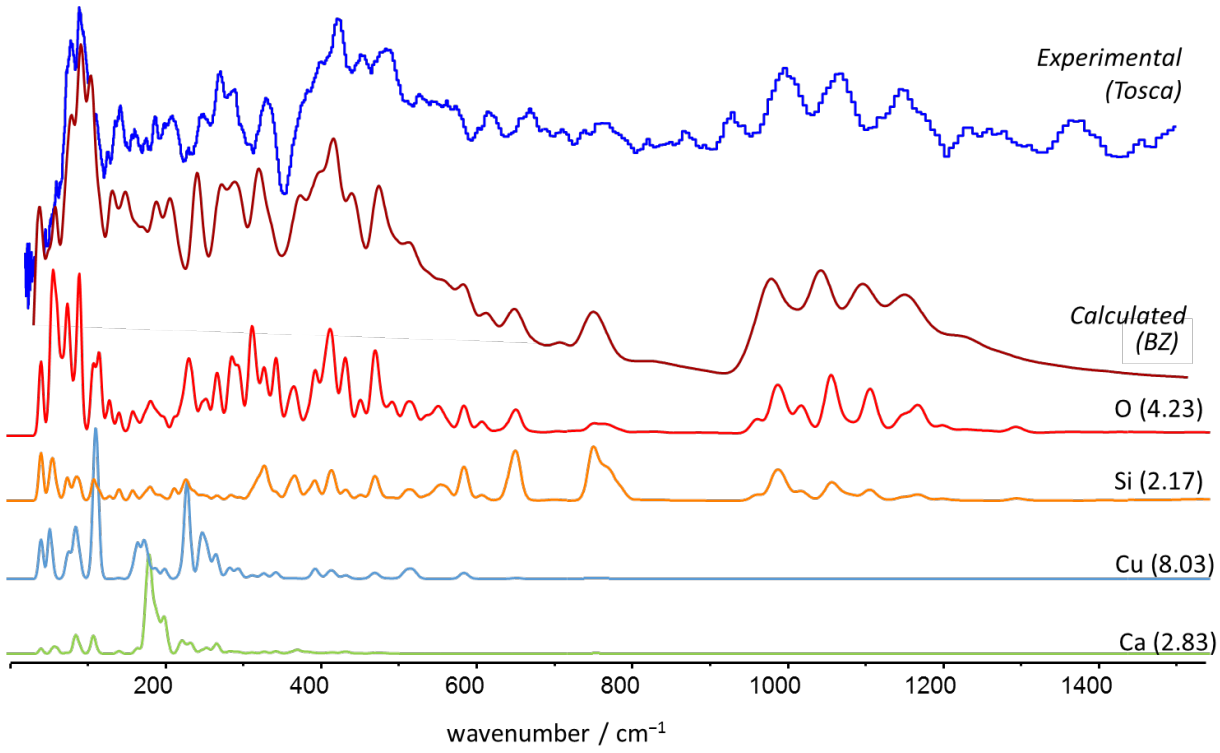

Fig. 12: Experimental INS/TOSCA spectrum of Egyptian blue up to 1500 cm^{-1} (blue line) compared with the calculated spectrum, averaged by the dispersion throughout the Brillouin zone, obtained with AbINS (BZ, magenta line). The four bottom lines (red to green) display the atomic contribution to the total INS spectrum (the nuclei neutron scattering cross section, in barn, is shown within brackets).

References

[1] Coimbra, M. M. *et al.* Shedding Light on Cuprorivaite, the Egyptian Blue Pigment: Joining Neutrons and Photons for a Computational Spectroscopy Study. *Cryst. Growth Des.* **23** (2023), 4961–4969. DOI: 10.1021/acs.cgd.3c00211

Dynamics of Furanosides: Theoretical and Experimental Spectroscopic Study of Methyl-β-D-Ribofuranoside

Matei Pascariu[1,2], Leonardo Bernasconi[3], Matthew Krzystyniak[1], James Taylor[1] and Svemir Rudić[1]

1. ISIS Neutron and Muon Source, UKRI STFC
2. Department of Chemistry, The University of Manchester,
3. Center for Research Computing & Department of Chemistry, University of Pittsburgh, United States

Furanosides, which are cyclic forms of monosaccharides containing a furan ring, are important components in various biological systems. Methyl-*β*-D-ribofuranoside, a derivative of ribose, serves as a model compound for understanding the structural and vibrational properties of furanosides and the motivation for studying this specific molecule is twofold: firstly, this is the simplest *β*-ribofuranoside of biological significance, and secondly, there is a lack of experimental and theoretical data for this molecule in the literature. This work, therefore, provides a detailed analysis of the said molecule using a combination of spectroscopic techniques and advanced computational methods to elucidate its electronic and vibrational characteristics.

To achieve a more robust understanding of the vibrational signatures of methyl-*β*-D-ribofuranoside, we not only employed three complementary spectroscopic techniques: inelastic neutron scattering (INS), infrared (IR) spectroscopy, and Raman spectroscopy, but we also simulated the resulting spectra of each technique. INS, particularly effective for studying hydrogen modes due to the high incoherent neutron cross-section of hydrogen nuclei, provided a complete vibrational spectrum without the constraints of optical selection rules. This was followed by IR and Raman spectroscopy, which offered additional insights into specific vibrational modes at mid-to-high energies that are better resolved with optical techniques.

The theoretical framework for this study was grounded in density functional theory (DFT) calculations, which were instrumental in interpreting the experimental data and understanding the vibrational spectra of methyl-*β*-D-ribofuranoside. All computational tasks were executed on the SCARF cluster. We utilized three distinct DFT approaches: gas-phase simulations with Gaussian 16, condensed-phase simulations using Gaussian basis sets with CRYSTAL 17, and condensed-phase simulations using plane-wave basis sets with CASTEP 23.

The DFT calculations provided detailed theoretical spectra that were in good agreement with the experimental INS, IR, and Raman spectra. Two distinct structures of the molecule were identified in the unit cell, differentiated mainly by the orientation of the furanose ring O−H bonds. The low-energy region of the spectrum (<400 cm^{-1}) is dominated by lattice vibrations and functional group rotation, while the mid-energy region is dominated by out-of-plane bending motions of the furanose ring (400−900 cm^{-1}) and by C−H bending in the methyl and methylene groups (1400−1600 cm^{-1}). The high-energy region (>2800 cm^{-1}) encompasses the C−H and O−H stretching modes and offers convincing evidence of at least one H-bonding interaction between the two structures of methyl-*β*-D-ribofuranoside.

Ultimately, the study demonstrates the effectiveness of combining advanced computational methods with diverse spectroscopic techniques to analyse complex molecular systems. The results fill a gap in the existing literature on ribofuranoside and suggest a more direct framework for using computational simulations as aids in spectral interpretation. The

computational resources provided by the SCARF cluster were pivotal in achieving these comprehensive results.

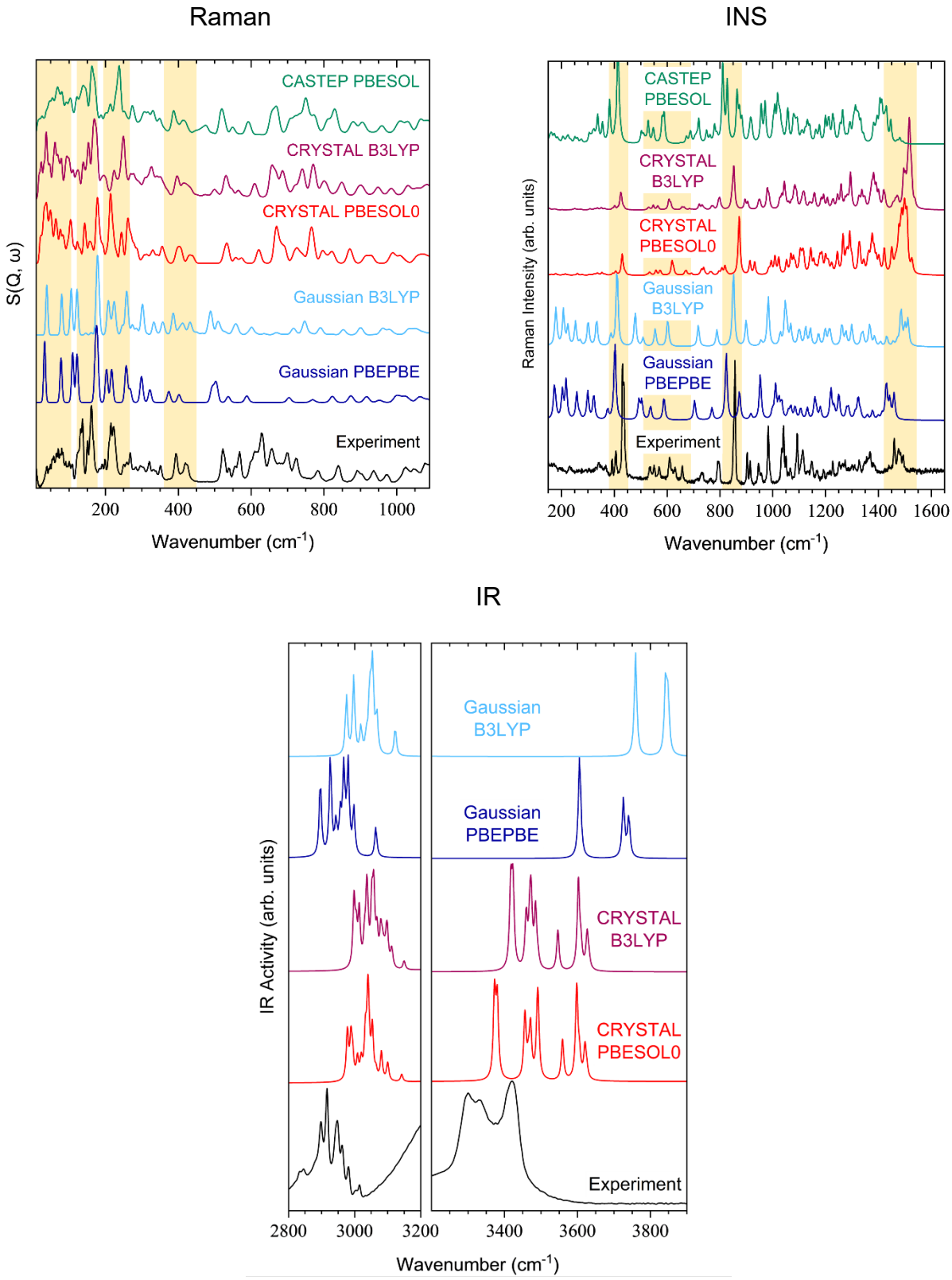

Fig. 13: Comparison between the experimental and simulated INS (top left), Raman (top right), and IR (bottom) vibrational spectra of methyl-*β*-D-ribofuranoside. Images are taken from M. Pascariu et al., J. Phys. Chem. A 128, 2111 (2024).

Presentations

This work has been presented as a poster at two conferences:

	Conference	Title	Presenter
1	European Conference on Neutron Scattering 2023, Garching, Germany	Dynamics of Furanosides: Inelastic Neutron Scattering and Raman Study of Methyl-β-D-Ribofuranoside	M. Pascariu
2	UK Neutron & Muon Science and User Meeting (NMSUM) 2023, Warwick, United Kingdom	Raman and Inelastic Neutron Scattering Study of the Dynamics of Methyl-β-D-Ribofuranoside	M. Pascariu

Publications

This work has been conducted during the year of 2023, but the publication related to it finally came out in February 2024:

M. Pascariu, L. Bernasconi, M. Krzystyniak, J. Taylor, and S. Rudić, *J. Phys. Chem. A*, 2024, **128**, 2111-2120.

Genome analysis of pathogenic E. coli strains

Martyn Winn[1], Sony Malhotra[1], Nicola Holden[2] and Ashley Ward[2]

1. Scientific Computing, UKRI STFC
2. Scotland's Rural College

Shigatoxigenic *Escherichia coli* (STEC) are notorious foodborne and zoonotic pathogens that are considered a priority public health risk. STEC can be classified by their serology, the most well-known being O157:H7. In recent years, an increasing number of clinical infections have been caused by non-O157 STEC, although not all STEC are capable of causing pathology. Testing laboratories need to undertake additional steps to identify the pathogen and assign it to a risk matrix.

In a scoping project funded by the STFC Food Network+, members of Scientific Computing's Computational Biology group collaborated with researchers from Scotland's Rural College (SRUC) to determine the feasibility of using computational approaches to distinguish pathogenic STEC. Data from DNA sequencing of bacterial isolates were obtained from collaborators. Some were from clinical isolates and known to cause disease, while others were from food sources or wild deer populations. Several computational tools were applied to these datasets to investigate the genetic make-up of clinical vs non-clinical isolates.

The primary data consisted of "reads" obtained from DNA sequencing, with a few million reads from each of 281 isolates, totalling approximately 250GB. The need to process this data through complex bioinformatics pipelines requires significant compute and storage, and was performed on SCARF between February and October 2022. The workflow is extremely heterogenous, but often involves large memory requirements and significant i/o to disk.

While only a short project, the work highlighted the genetic variation in *E. coli* strains and the need for a more detailed understanding of this. Results were presented at a community workshop in August 2022, attended by representatives from public health agencies and reference laboratories. The work was also presented as a Case Study https://www.scd.stfc.ac.uk/Pages/Can-my-cheeseburger-harm-me.aspx to highlight the relevance of computational science to real-world concerns.

On the basis of this scoping project, a follow-up project was funded by the UK Food Safety Research Network, based at the Quadram Institute in Norwich. The first study had revealed a large variation in the presence of virulence genes (see Figure 14) as well as allelic variation within a given gene. The new project is studying the latter in more detail, and linking mutations to function via structural modelling. We have linked up with PrimerDesign based in Southampton, with the long-term aim to develop diagnostic tests based on knowledge gained of the genetic make-up of pathogenic strains.

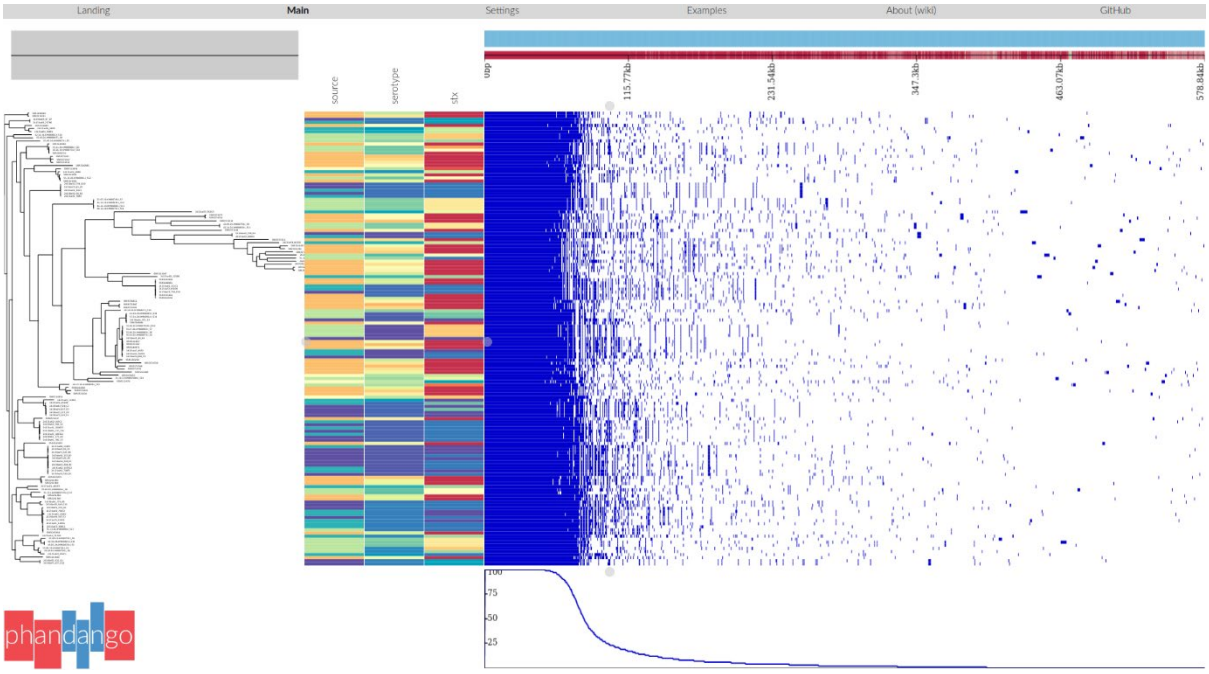

Fig. 14: Results of a pangenome analysis using Roary and displayed by Phandango. The left-hand side shows a phylogenetic tree of 147 genomes of STEC isolates. The right hand side shows the genes shared by these isolates, with core genes occurring in all isolates (solid blue columns) and cloud genes such as virulence genes occurring in only some (sparse blue columns).

The heating of hot electrons produced at sub-relativistic intensities

R. A. B. Alraddadi[1], A. P. L. Robinson[2], Raoul M. G. M Trines[2] and N. C. Woolsey[3]

1. Physics Department, Science Colleges, King Saud University, Saudi Arabia.
2. Central Laser Facility, UKRI STFC
3. York Plasma Institute, Department of Physics, University of York

Understanding the physical mechanisms of laser-generated-fast-electron- heating is crucial for different areas of high energy density physics. As MeV energetic electrons have their limitations in the term of plasma heating [1, 2], we proposed alternative fast-electron-heating approach supported by analytic method [3]. Our approach uses lower energy ‘hot’ electrons in the range of 20 keV to 100 keV that can be produced at sub-relativistic intensities.

We use SCARF-derevolutionibus resources to run sets of two-dimensional PIC simulations, namely EPOCH code to estimate the required conditions for such heating. Hot electrons are generated via inducing Two-Plasmon Decay (TPD) instabilities [kruer2019physics]. Figure 15 shows the emerging of TPD instability where electron jets features with 45°. We found that 10% of the absorption fraction and 30 keV are enough to boost hot electron heating and longer density scale length is needed to increase absorption fraction.

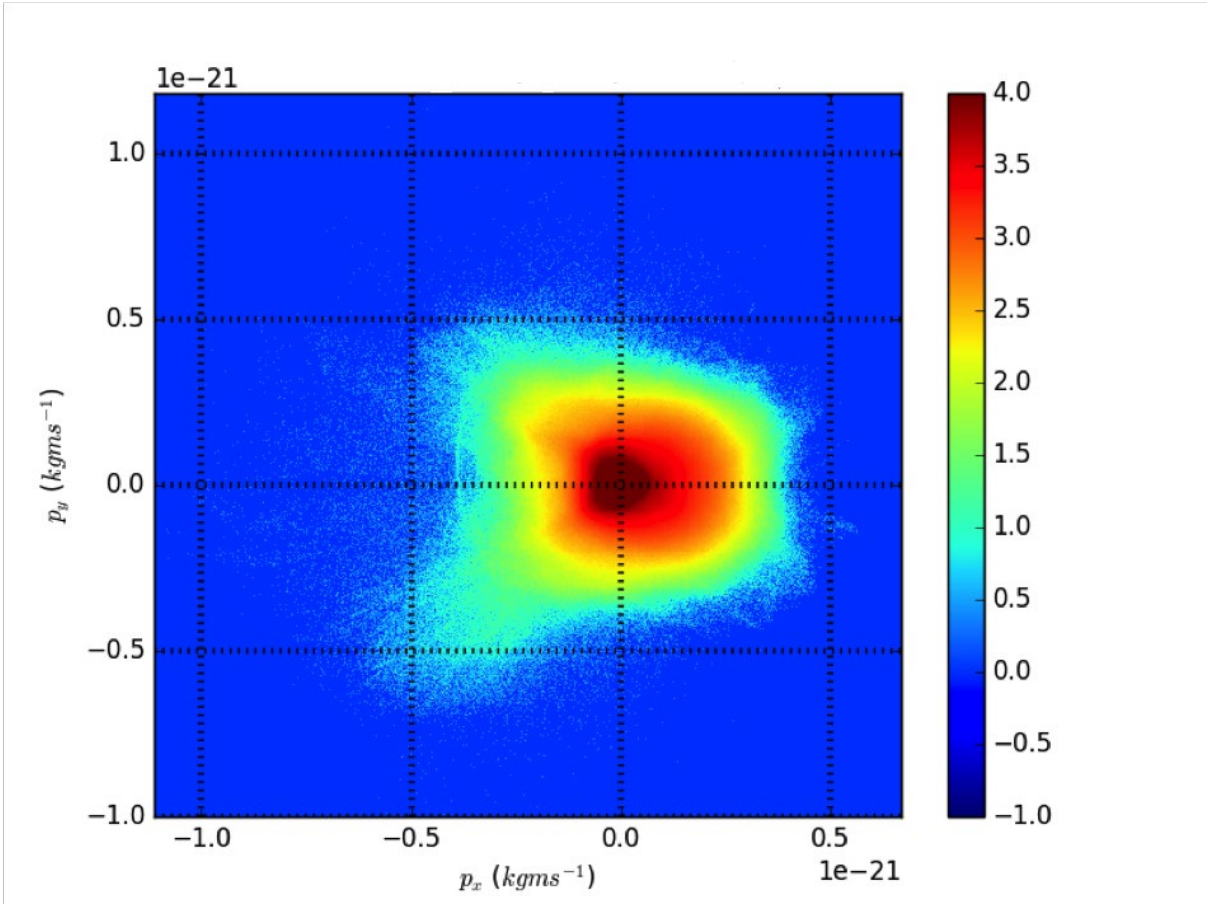

Fig. 15: The electron phase-space plot px-py.

References

[1] A. R. Bell et al, *Plasma Phys.Control. Fusion*, 39, 653 (1997).
[2] P. Patel et al, *Physical review letters*, 91, 125004 (2003).
[3] R. A. B. Alraddadi, A. P. L. Robinson, Raoul M. G. M Trines, and N. C. Woolsey, *Phys. Plasmas*, to be submitted (2024).
[4] W. Kruer, The physics of laser plasma interactions, (crc Press, 2019)

Salt Effect on Donnan Equilibrium in Montmorillonite Demonstrated with Molecular Dynamics Simulations

Ya-Wen Hsiao[1], Magnus Hedström[2]

1. Scientific Computing Department, UKRI STFC
2. Clay Technology, Sweden

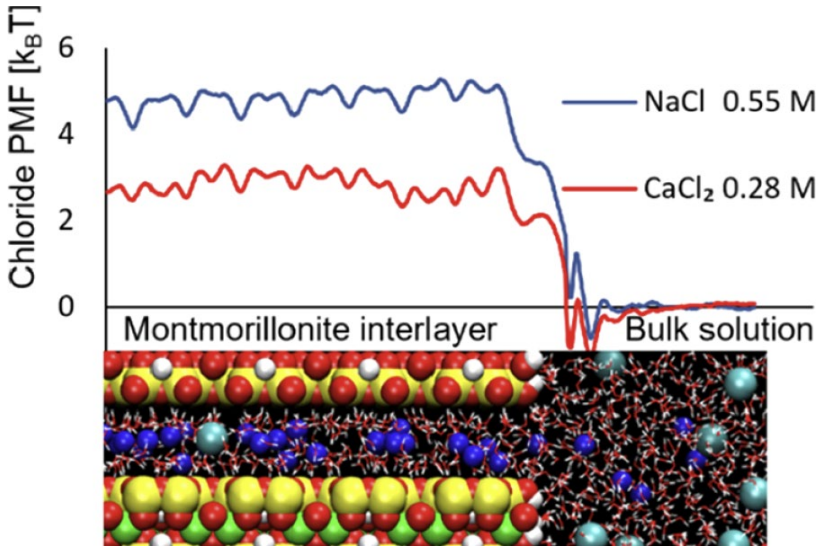

Fig. 16: In CaCl2, the PMF of chloride is lower in the interlayer compared with that of NaCl at similar external Cl- concentration.

Donnan equilibrium governs the distribution of ions in many systems such as ion exchange membranes and biological cells in contact with an external electrolyte. Herein, Donnan equilibrium between bulk salt solution and bihydrated montmorillonite was investigated because such a system is of great importance for many nuclear waste disposal concepts.

Specifically, we used molecular dynamics simulations to determine the partition coefficient of chloride, which was achieved by calculating the free-energy difference of chloride in the interlayer and the bulk using enhanced sampling methodology. Montmorillonite in equilibrium with either NaCl or $CaCl_2$ was examined to elucidate the general difference between 1:1 and 2:1 salts. The concentration dependence of the partition coefficient for each salt was determined using three and four concentrations for NaCl and $CaCl_2$, respectively.

In the case of NaCl, we found that the partition coefficient increased linearly with the concentration, while for $CaCl_2$, the increase was proportional to the square root of the concentration. A derivation of the partition coefficient using general Donnan theory that includes excess free energy contributions beyond the electrostatic Donnan potential is also presented. For both salts, the agreement between the partition coefficient from the simulations and Donnan theory was excellent. Although Donnan theory is a continuum theory derived without any reference to atomistic details, the present results justify its application to systems with nanoscale pores.

This work was published in J. Phys. Chem. B 2022, 126, 8873−8881.

Structure adaptation in Omicron SARS-CoV-2/hACE2: Biophysical origins of evolutionary driving forces

Ya-Wen Hsiao[1,2], David J. Bray[1], Tseden Taddese[1], Guadalupe Jimenez-Serratos[1], and Jason Crain[3,4]

1. The Hartree Centre, UKRI STFC
2. Scientific Computing, UKRI STFC
3. IBM Research Europe, Hartree Centre
4. Department of Biochemistry, University of Oxford

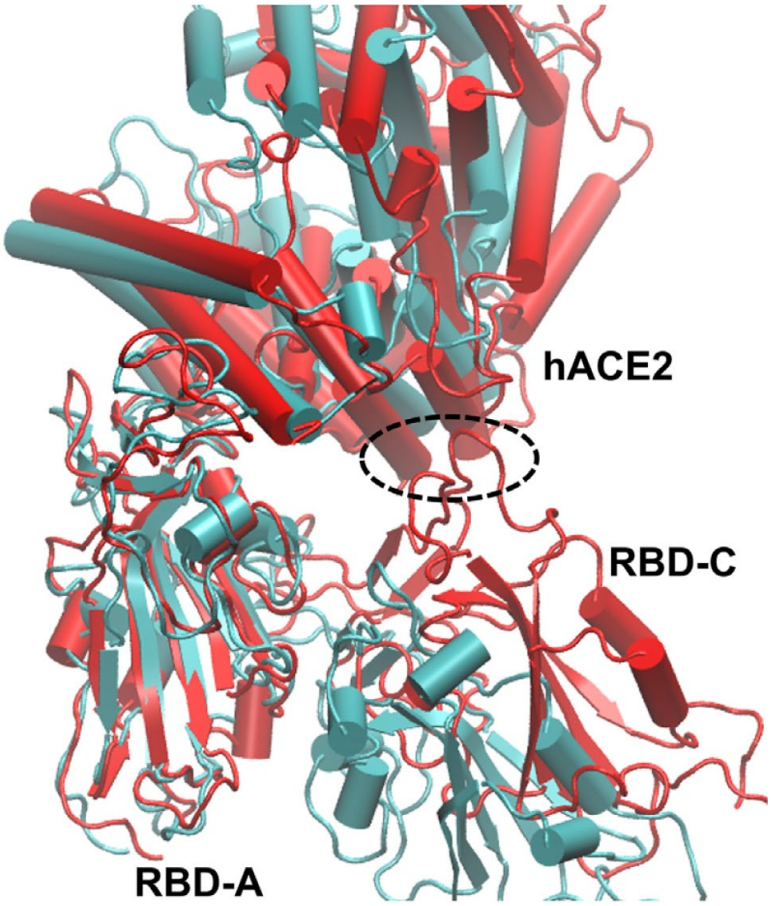

Fig. 17: S+hACE2 complexes involving WT (cyan) and BA.2 (red) aligned with RBD-A, showing that RBD-C of BA.2 is drawn closer to hACE2 (with interaction at the location of the dashed circle).

Since its emergence, the COVID-19 threat has been sustained by a series of transmission waves initiated by new variants of the SARS-CoV-2 virus. Some of these arise with higher transmissivity and/or increased disease severity.

Here, we use molecular dynamics simulations to examine the modulation of the fundamental interactions between the receptor binding domain (RBD) of the spike glycoprotein and the host cell receptor (human angiotensin-converting enzyme 2 [hACE2]) arising from Omicron variant mutations (BA.1 and BA.2) relative to the original wild-type strain.

Our key findings are that glycans play a vital role at the RBD…hACE2 interface for the Omicrons, and the interplay between glycans and sequence mutations leads to enhanced

binding. We find significant structural differences in the complexes, which overall bring the spike protein and its receptor into closer proximity. These are consistent with and attributed to the higher positive charge on the RBD conferred by BA.1 and BA.2 mutations relative to the wild-type. However, further differences between subvariants BA.1 and BA.2 (which have equivalent RBD charges) are also evident: mutations reduce interdomain interactions between the up chain and its clock-wise neighbour chain in particular for the latter, resulting in enhanced flexibility for BA.2.

Consequently, we see occurrence of additional close contacts in one replica of BA.2, which include binding to hACE2 by a second RBD in addition to the up chain. Although this motif is not seen in BA.1, we find that the Omicrons can directly/indirectly bind a down-RBD to hACE2 through glycans: the role of the glycan on N90 of hACE2 switches from inhibiting to facilitating the binding to Omicron spike protein via glycan-protein lateral interactions.

These structural and electrostatic differences offer further insight into the mechanisms by which viral mutations modulate host cell binding and provide a biophysical basis for evolutionary driving forces.

This work was published in Biophysical Journal 122, 4057–4067, October 17, 2023

APPENDIX A: SCARF HARDWARE DETAILS

CPU Nodes

Host group	CPU	Nodes	Cores /node	Total cores	Interconnect	Total mem (GB)
SCARF 23	AMD EPYC 7502	132	32	4224	HDR Infiniband	33792
SCARF 22	AMD EPYC 7502	32	32	1024	HDR Infiniband	8192
SCARF 21	AMD EPYC 7502	168	32	5376	HDR Infiniband	43008
SCARF 20	AMD EPYC 7502	78	32	2560	EDR Infiniband	21504
SCARF 19	Intel Xeon Gold 6126	16	24	384	EDR Infiniband	3072
SCARF 18	Intel Xeon Gold 6126	148	24	3552	EDR Infiniband	28416
SCARF 17/ DeRevolutionIbus	Intel E5-2650 v4	201	24	4824	EDR Infiniband	25728
SCARF 16/ MagnaCarta/ IBIS	Intel E5-2650 v3	56	20	1120	FDR Infiniband	7168
Total		**699**		**23064**		**170,880**

GPU Nodes

Host group	CPU	GPU	Nodes	Cores /node	Total cores	Interconnect
SCARF 23	AMD 7302	NVIDIA A100x4	6	32	192	HDR Infiniband
SCARF 21	**AMD 7302**	**NVIDIA A100x4**	**6**	**32**	**192**	**HDR Infiniband**

APPENDIX B: PUBLICATIONS AND PRESENTATIONS

Publications

Title	Authors	Journal
Ab initio study of structural, elastic and thermodynamic properties of Fe3S at high pressure: Implications for planetary cores.	K. Valencia, A. de Moya, G. Morard, N. L. Allan and C. Pinilla	American Mineralogist, 107, 248-256 (2022)
Signature of a randomness-driven spin-liquid state in a frustrated magnet	J. Khatua, M. Gomilšek, J. C. Orain, A. M. Strydom, Z. Jagličić, C. V. Colin, S. Petit, A. Ozarowski, L. Mangin-Thro, K. Sethupathi, M.S. Ramachandra Rao, A. Zorko and P. Khuntia	To appear in Comm. Phys. (2022).
Effect of Internal Donors on Raman and IR Spectroscopic Fingerprints of $MgCl_2/TiCl_4$ Nanoclusters Determined by Machine Learning and DFT	M. D'Amore*, T. Taniike, M. Terano, A. M. Ferrari	Materials, 2022, 15 (3), 909.
One-dimensional hydrodynamic simulations of low convergence ratio direct-drive inertial confinement fusion implosions	R. W. Paddock et al.	Philosophical Transactions of the Royal Society A: Mathematical, Physical and Engineering Sciences, **379**, 20200224 (2021).
Pathways towards break even for low convergence ratio direct-drive inertial confinement fusion	R. W. Paddock et al.	Journal of Plasma Physics, **88**, 905880314 (2022).
Energy gain of wetted-foam implosions with auxiliary heating for inertial fusion studies	R. W. Paddock et al.	R. W. Paddock et al., "Energy gain of wetted-foam implosions with auxiliary heating for inertial fusion studies", Plasma Phys. Control. Fusion, **66,** 025005 (2024).

Presentations

Conference	Title	Presenter
April 18-20 2022, *Materials Science & Engineering,* Boston (USA)	Revisiting the identity of δ-MgCl2: structure and properties of nanoclusters by DFT, spectroscopy and machine learning. How modelling uncovers the origin of industrial catalysis	Maddalena D'Amore, G. Takasao, T. Wada, T. Taniike, A. Piovano, P. C. Bruzzese, P. Chammingkwan, F. Pascale, E. Groppo, B. Civalleri, M. Terano, S. Bordiga, A. M. Ferrari
CATCHEM, June 20-21, 2022 Berlin (Germany)	Revisiting the identity of δ-$MgCl_2$: structure and properties of nanoclusters by DFT, spectroscopy and machine learning. How modelling uncovers the origin of industrial catalysis	Maddalena D'Amore, G. Takasao, H. Chikuma, T. Wada, T. Taniike*, A. Piovano, P. C. Bruzzese, P. Chammingkwan, F. Pascale, E. Groppo, B. Civalleri, M. Terano, S. Bordiga, A. M. Ferrari
IPAC'21, Campinas, SP, Brazil, May 2021	Second Beam Test and Numerical Investigation of the Imperial College Plasma (Gabor) Lens Prototype	Dascalu, T.-S. et al.
Direct Drive and Fast Ignition Workshop, 2022	Investigating wetted foam capsules for inertial fusion energy	R.W. Paddock
American Physical Society Division of Plasma Physics 2021, 2023	Investigating wetted foam capsules for inertial fusion energy	R.W. Paddock
European Conference on Neutron Scattering 2023, Garching, Germany	Dynamics of Furanosides: Inelastic Neutron Scattering and Raman Study of Methyl-β-D-Ribofuranoside	M. Pascariu
UK Neutron & Muon Science and User Meeting	Raman and Inelastic Neutron Scattering Study of the	M. Pascariu

(NMSUM) 2023, Warwick, United Kingdom	Dynamics of Methyl-β-D-Ribofuranoside	

APPENDIX C: SCARF USAGE 2022-23

General SCARF Queues

Unsurprisingly, of the non-restricted queues, usage of the scarf queue dominates. The Preemptable queue allows users to run across all hardware (including that which is normally restricted) with the caveat that the job may be ended if the nodes are required by a job in another queue that the hardware normally prioritises. The devel queue is intended for short interactive workloads.

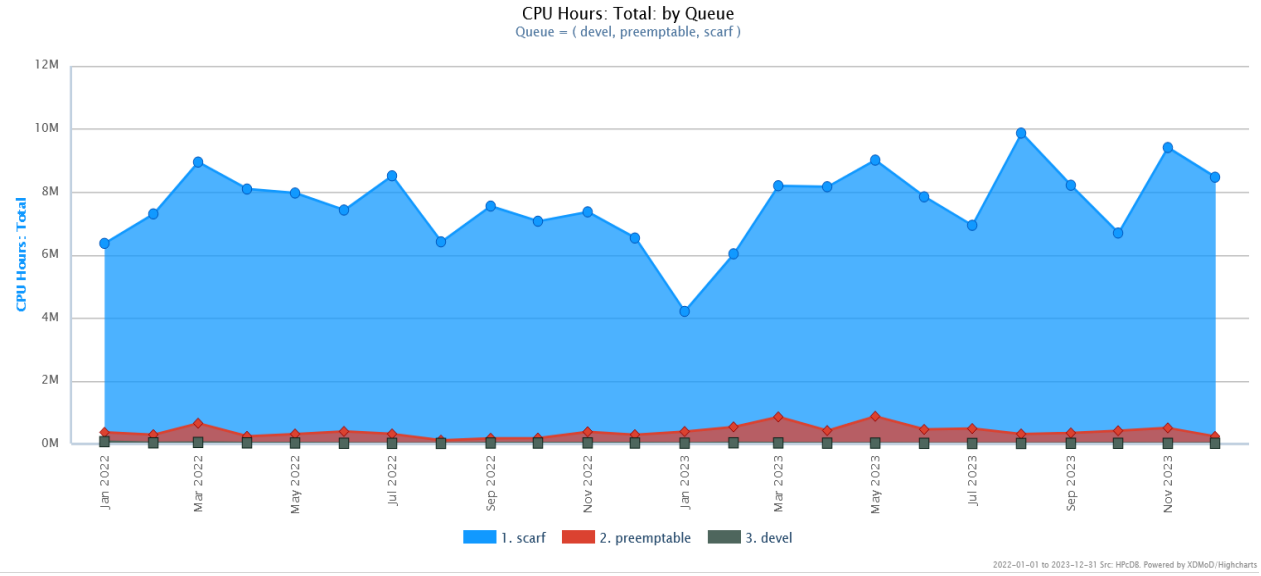

Fig. 18: SCARF Queue Usage

MagnaCarta, DeRevolutionibus and Demagnate

These queues are primarily for CLF Plasma Physics use. MagnaCarta has 480 cores purchased in 2016. DeRevolutionibus has 1608 cores purchased in 2017. Demagnate has 384 cores and was purchased in 2019.

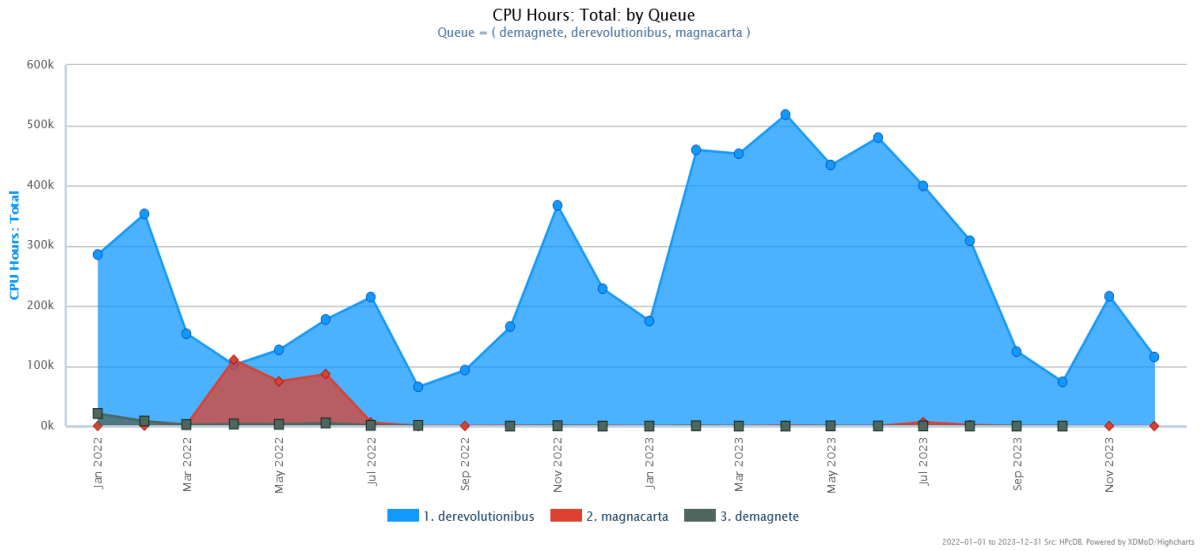

Fig. 19: SCARF-MagnaCarta, DeRevolutionibus and Demagnate Usage

DeRevolutionibus continues to be used for higher priority MagnaCarta users and on demand to support CLF experiments.

SCARF-IBIS

SCARF-IBIS has a capacity of 240 CPU cores and are used for the *Intense Beams in Synchrotrons* collaboration.

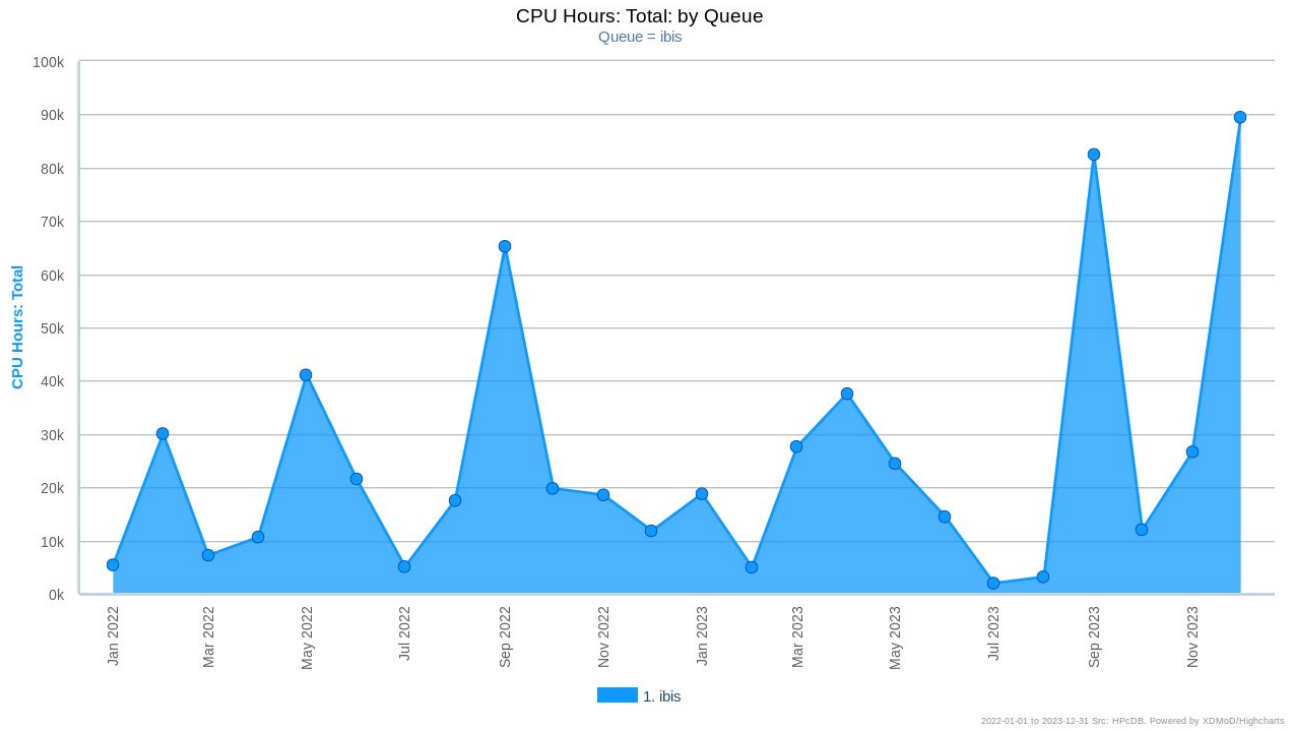

Fig. 20: SCARF-IBIS Usage

SCARF Total Power draw

The approximate average power draw of the SCARF cluster for 2022/2023 was 700 amps or 170 kW, excluding the power needed to cool, pump and move cold air.

Filesystem Usage

The bulk of the storage used by SCARF is provided by the Panasas storage system. As of the end of 2023, approximately 1PB was being used out of a total of 2.4PB available.

Networking

The diagram below shows the SCARF compute clusters embedded in the larger Research Infrastructure group's networking infrastructure.

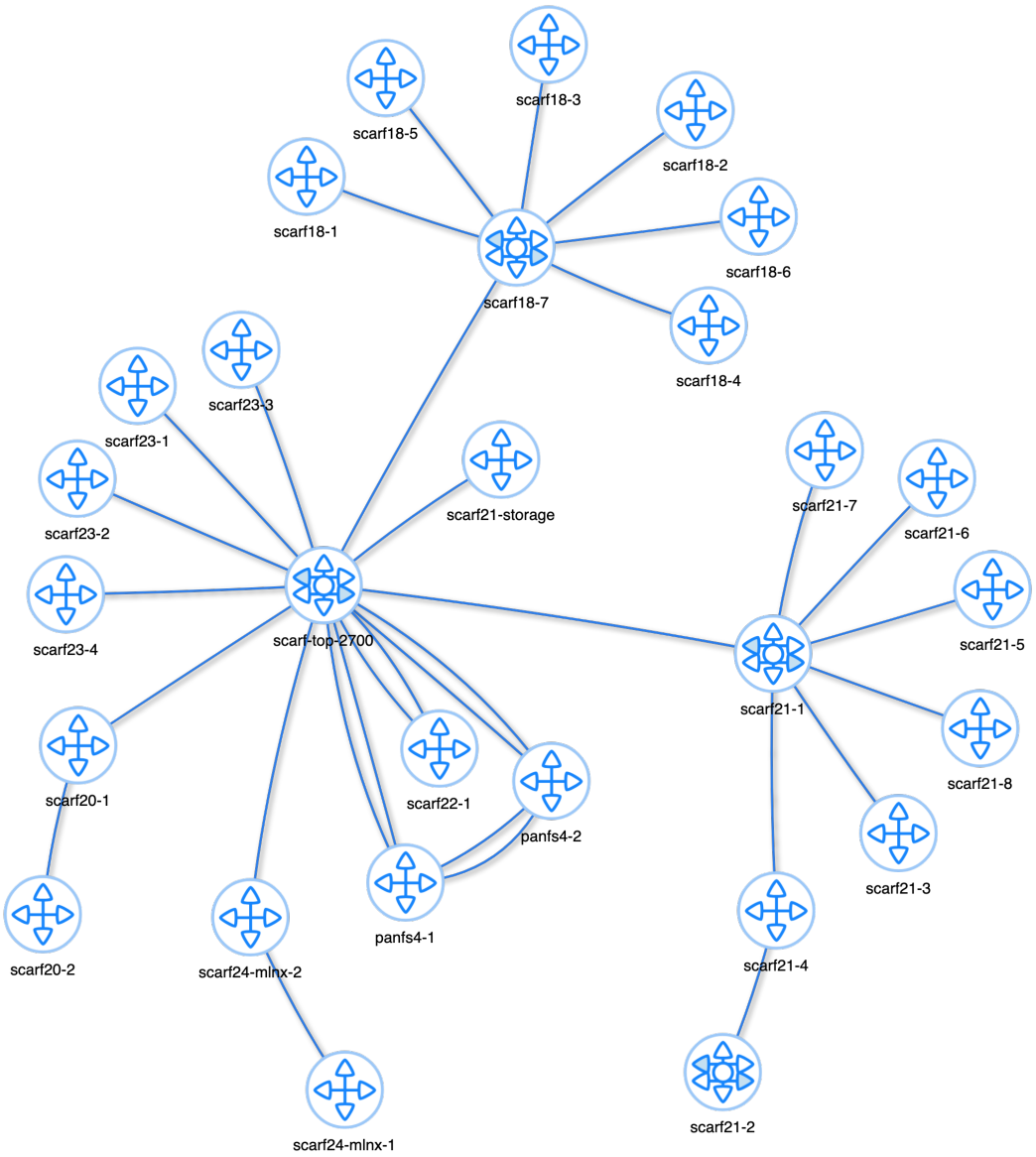

Fig. 21: SCARF Network Topology